A&A 424, 719–726 (2004)
DOI: 10.1051/0004-6361:20035849


Astronomy & Astrophysics

# First observations with an *H*-band integrated optics beam combiner at the VLTI⋆

J. B. LeBouquin[1], K. Rousselet-Perraut[1], P. Kern[1], F. Malbet[1], P. Haguenauer[1], P. Kervella[2], I. Schanen[3], J. P. Berger[1], A. Delboulbé[1], B. Arezki[1], and M. Schöller[2]

[1] LAOG – Laboratoire d'Astrophysique UMR UJF-CNRS 5571, Observatoire de Grenoble, Université Joseph Fourier, BP 53, 38041 Grenoble Cedex 9, France
e-mail: jean-baptiste.lebouquin@obs.ujf-grenoble.fr
[2] ESO – European Southern Observatory, Casilla 19001, Santiago 19, Chile
[3] IMEP – Institut de Microélectronique Electromagnétisme et Photonique, 38016 Grenoble Cedex 1, France

Received 11 December 2003 / Accepted 29 March 2004

**Abstract.** This paper reports results obtained with the Very Large Telescope Interferometer Commissioning Instrument (VLTI-VINCI) where the fiber interferometric coupler MONA was temporarily replaced by an integrated optics beam combiner (IONIC). The two-beam combiner operating in the *H* atmospheric band was tested at Paranal during two weeks in July 2002. Fringes were recorded on several stars with the siderostats and the Unit Telescopes (UT). We demonstrate that integrated optics allows beam combination with a high interferometric efficiency, stability and spatial filtering. The instrumental visibility of VLTI+IONIC is better than 85%, which is just 5% under the visibility of the IONIC device alone. During this run, the flux injection in the IONIC combiner was not optimized since we used the *K*-band MONA optics. However, we obtain fringes with the 35 cm siderostats on a star of magnitude $mH = 2.47$ ($\kappa^2$ Scl). It allows us to extrapolate a magnitude around $mH \sim 6$ with 8 m telescopes without adaptive optics and in the same poor injection conditions.

**Key words.** techniques: interferometric – methods: data analysis – instrumentation: interferometers

## 1. Introduction

The Very Large Telescope Interferometer (VLTI, Glindemann et al. 2003) is a multi aperture optical array that provides high sensitivity. The first generation of instruments includes a two-beam combiner in the thermal infrared MIDI (Leinert et al. 2003) and a three-beam combiner in the $J, H, K$ bands AMBER (Petrov et al. 2003). VINCI is the VLT INterferometer Commissioning Instrument, which combines two beams in the $K$ band by means of a fluoride glass fiber coupler (Kervella et al. 2003a). The precise calibration due to single-mode fibers and photometric calibration has demonstrated its excellent capability (Domiciano de Souza et al. 2003; Ségransan et al. 2003; di Folco et al. 2003; Pijpers et al. 2003; Kervella et al. 2003b). In the future, the goal is to recover the interferometric information of the entire array in order to have imaging ability with a spatial resolution of one milliarcsecond in the near infrared. The main problem will be the complexity of the focal combination scheme. For example, using classical bulk optics, it takes $N(N-1)/2$ beam-splitters to combine $N$ beams in a coaxial pairwise scheme. Each optical element decreases the global transmission and efficiency of the instrument. The whole optical assembly of the beam combiner must maintain an internal stability crucial for closure phase measurement, which is the information necessary for image reconstruction.

Over the last years, the Laboratoire d'Astrophysique de Grenoble (LAOG), in collaboration with IMEP and LETI developed the integrated optics beam combiner (IONIC). The stability and compactness of these planar optical wave guides represent significant advantages of this technology. It has been sucessfully tested in the laboratory (Haguenauer et al. 2000) and on the sky for the two-beam (Berger et al. 2001) and three-beam combination (Berger et al. 2003).

A two-beam IONIC combiner was tested at the VLTI during two weeks in July 2002, and fringes were obtained on several stars. The first objective of this run was to give access to the *H*-band for the VLTI commissioning and scientific exploitation. The second was to test a integrated optics combiner in the VLTI environment to prepare future multi-telescope instrumentation or facilities (Kern et al. 2003). We discuss the stability of the beam combiner, the modal filtering ability of integrated optics and the global interferometric efficiency of the instrument.

⋆ Based on observations collected at the European Southern Observatory, Paranal, Chile (public commissioning data).

**Table 1.** Throughput measured at 1.55 $\mu$m (laser source) for unpolarized light of the integrated optics combiner before and after connecting performed by the GeeO company. The "–" denotes that measurements have not been done.

| | Before connecting | | After connecting | | Theoretical | |
|---|---|---|---|---|---|---|
| Injection in input | *A* | *B* | *A* | *B* | *A* | *B* |
| Throughput on $P_a$ | 39% | – | 36% | – | 50% | 0% |
| Throughput on $P_b$ | – | 39% | – | 35% | 0% | 50% |
| Throughput on *I* | 17% | 17% | – | – | 25% | 25% |
| Total throughput | 56% | 56% | – | – | 75% | 75% |
| Photometric ratio | 0.44 | 0.44 | – | – | 0.5 | 0.5 |

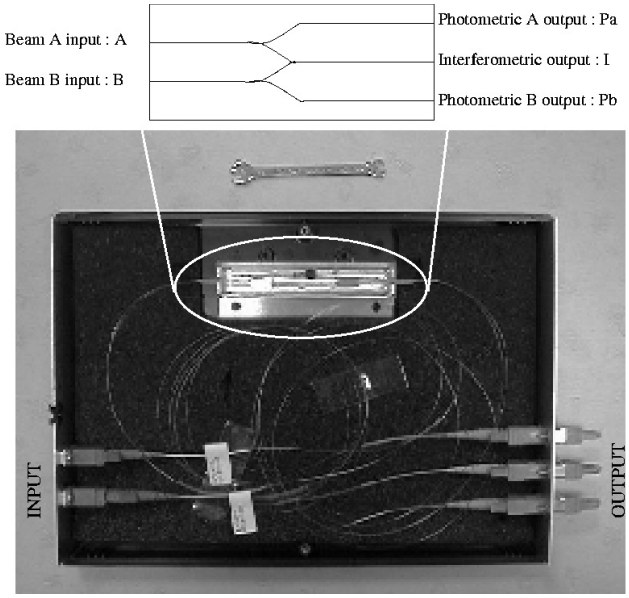


**Fig. 1.** *Top*: design of the integrated optics two-beam combiner. *Bottom*: the connected combiner in its box at ESO.

## 2. Instrumentation

### 2.1. Integrated optics beam combiner

The two-telescope beam combiner (Fig. 1) ensures the following functions:

- modal filtering throughout the *H* band due to single-mode waveguides whose cut-off wavelength is shorter than 1.4 $\mu$m;
- combination of two input beams by means of a reverse *Y* junction similar to a beam-splitter (see Malbet et al. 1999 for a complete description of the existing integrated optics functions);
- photometric calibration due to *Y* junctions that split the input flux between the interferometric output (*I*) and the photometric outputs (*Pa*, *Pb*).

The beam combiner was manufactured by the GeeO[1] company (Grenoble, France) with a silver ion-exchange technology. It is connected via polarization-maintaining singlemode fibers at each end. All the fibers have E2000 connectors from the Diamond company to be compliant with the VINCI interface. For each output *Y*, throughput is defined as the ratio between the number of photons detected at the output and the number of photons injected in the input *X*:

$$\tau_{X\to Y} = \frac{Nb\gamma(Y)}{Nb\gamma(X)}. \quad (1)$$

The total throughput for each input corresponds to:

$$\tau_A = \tau_{A\to P_a} + \tau_{A\to I} + \tau_{B\to P_b}$$
$$\tau_B = \tau_{B\to P_a} + \tau_{B\to I} + \tau_{B\to P_b}. \quad (2)$$

Since the component is symmetric and because the reverse *Y*-junction introduces a loss of half of the flux, the theoretical throughputs are 50% for $\tau_{A\to P_a}$ and $\tau_{B\to P_b}$ and 25% for $\tau_{A\to I}$ and $\tau_{B\to I}$. Throughputs of the component alone have been measured before connecting (Table 1, Col. 2). Light is injected and collected at the output by fibers whose transmission are calibrated and subtracted. Throughputs of the component+fibers are then measured after connecting (Table 1, Col. 3). The total throughputs ($\tau_A$ and $\tau_B$) exceed 50% and are equal at the percent level.

Contrasts have been measured with the LAOG testbench throughout the *H* band with the beam combiner connected at both ends. The contrasts equal about 90% and reach up to 97% with a linear polarizer at the combiner output. This difference of a few percent shows that there is no drastic instrumental polarization. The slight difference can be explained by a small mismatch of the neutral axes between the optics of the LAOG testbench. The accuracy of the alignment of the neutral axes (especially for the fibers) has not been determined.

### 2.2. Implementation in the VLTI environment

Today, the VINCI instrument recombines two beams in the *K* band with a fluoride glass fiber coupler (MONA). The IONIC beam-combiner has been designed to be able to switch from MONA to the IONIC combiner easily, and therefore from the *K* to the *H* band. The E2000 connectors of the IONIC beam combiner inputs are connected at the focus of the MONA input off-axis parabola and the connectors of the IONIC beam combiner outputs are connected to the VINCI fiber bundle. No opto-mechanical modifications are required and the switch takes a few minutes. As a consequence, the global throughput of the IONIC instrument is reduced by a factor of ~1.5 since the MONA input off-axis parabola is not optimized for the numerical aperture of the IONIC fibers (0.13 compared to the numerical aperture of 0.23 of the K fluoride glass fibers). Minor

[1] www.geeo.com

**Table 2.** List of the targets observed at Paranal during July 2002 with IONIC and VINCI on the VLTI. The stellar angular diameters are extracted from the CHARM database (Richichi & Percheron 2002).

| Target name | No. of obs. | $mH$ [mag] | $mK$ [mag] | ⌀ [mas] |
|---|---|---|---|---|
| 24 Cap | 3 | 0.72 | 0.52 | 4.59 ± 0.27 |
| 58 Hya | 4 | 1.20 | 1.11 | 3.38 ± 0.19 |
| $\alpha$ Aql | 57 | 0.10 | 0.10 | 3.12 |
| $\alpha^1$ Cen | 3 | | | 8.31 ± 0.02 |
| $\alpha$ Eri | 42 | 0.86 | 0.88 | 1.91 ± 0.15 |
| $\alpha$ Ind | 81 | 0.77 | 0.69 | 3.86 ± 0.09 |
| $\alpha$ Psa | 32 | 0.937 | 0.94 | 2.39 ± 0.45 |
| $\beta$ Ori | 4 | 0.17 | 0.20 | 2.77 ± .03 |
| $\chi$ Phe | 10 | 1.80 | 1.56 | 3.69 ± 0.03 |
| $\epsilon$ Eri | 6 | 1.88 | 1.77 | 2.15 ± 0.06 |
| HR 6869 | 6 | 1.04 | 1.05 | 2.98 ± 0.03 |
| HR 74 | 2 | 1.09 | 1.03 | |
| HR 7652 | 10 | 1.70 | 1.57 | 2.69 ± 0.06 |
| HR 8685 | 1 | 2.16 | 1.96 | 2.10 ± 0.11 |
| $\kappa^2$ Scl | 3 | 2.47 | 2.39 | 1.86 ± 0.1 |
| $\lambda$ Sgr | 1 | 0.43 | 0.33 | 4.36 ± 0.21 |
| $\lambda$ Car | 2 | 1.18 | 1.04 | |
| $\tau$ Aqr | 1 | 0.42 | 0.31 | 5.36 ± 0.32 |

software changes were required because of the single interferometric output of the IONIC combiner (MONA has two interferometric outputs in opposite phase).

## 3. Observations and data reduction

### 3.1. Dataset

A total of 13 nights of observations covering 20 different stars were performed during the observing run (Table 2). The faintest star observed is $\kappa^2$ Scl, at $mH = 2.47$ (2002−07−28, with the siderostats). Only one night the Unit Telescopes were used (UT2 in Beam A and UT1 in Beam B). Fringes were obtained on $\alpha$ Aql. Each VINCI observing block is made of four acquisitions:

OFF-SOURCE: a dark signal acquisition, without light injection into the IONIC beam combiner; this dark signal was obtained by putting the shutters in front of the beams;

BEAM-A: a first calibration acquisition with light injection only in the $A$ combiner input, in order to calibrate the flux ratio ($\kappa_a$) between the interferometric output $I$ and the photometric output $P_a$ (see also Fig. 1 top);

BEAM-B: a second calibration acquisition with light injection only in the $B$ combiner input, in order to calibrate the flux ratio ($\kappa_b$) between the interferometric output $I$ and the photometric output $P_b$;

ON-SOURCE: a fringe acquisition, with injection in the two inputs $A$ and $B$.

Each acquisition (individual file) is composed of 20, 100 or 500 scans of the optical path delay around the zero OPD.

### 3.2. Data processing

For a variable $u$, we define its estimators $\widehat{u}$ and its Wiener filtering estimators $\widehat{u}^w$. In a first step, we calculate the dark level in the OFF-SOURCE file. $\widehat{P_a}$, $\widehat{P_b}$ and $\widehat{I}$ are the values at the three component outputs corrected from the dark.

#### 3.2.1. Interferometric to photometric ratio

We define $\kappa_i$ as the flux ratio between the photometric and the interferometric outputs for injection only in the associated beam. With an observation block, $\kappa_a$ and $\kappa_b$ could be determined in two different ways:

– with the ON-SOURCE file, by fitting the three light curves where $x$ is the optical path delay:

$$\widehat{I^w}(x) = \widehat{\kappa_a}.\widehat{P_a^w}(x) + \widehat{\kappa_b}.\widehat{P_b^w}(x); \tag{3}$$

– with the calibration files BEAM-A and BEAM-B by dividing the interferometric flux by the photometric one:

$$\widehat{\kappa_i} = \frac{\left\langle \widehat{I} \right\rangle}{\left\langle \widehat{P_i} \right\rangle}. \tag{4}$$

Because the inverse $Y$ junction combination introduces a loss of half of the flux in the interferometric waveguide, the theoretical value for $\kappa_i$ is 0.5. In this paper, we analyze the $\kappa_i$ values through three evolutionary times scales:

– the reading time of the sampling in the OPD scan (∼0.3 ms) which is faster than the turbulence fluctuation time (∼40 ms). It enables us to detect a possible correlation between the injection and the combiner properties;
– the time of an observation block (∼5 min). In this timescale, the stability of the combiner is very important because the $\kappa$ determined in the calibration acquisition is used in the next science acquisition;
– from night to night.

#### 3.2.2. Coherence factor

The data processing is illustrated with an example in Fig. 2. Let us define $x$ as the optical path delay and $\sigma$ the wavenumber. The relation between the different quantities for a single-mode interferogram is given by:

$$I(x) = \kappa_a.P_a(x) \; + \; \kappa_b.P_b(x) + I_{\rm HF} \tag{5}$$

with:

$$I_{\rm HF} = \underbrace{2.\sqrt{\kappa_a.P_a(x).\kappa_b.P_b(x)}}_{C} \; . \; \mu.I_c(x) \tag{6}$$

where:

– $C$ is the coherent flux;
– $I_c(x)$ is the real part of the Fourier transform of the normalized spectral response of the interferometer $T(\sigma)$ (product of $H$-band filter transmission by the star spectrum). Since the integral of $T$ is normalized to one, we have $I_c(0) = 1$;

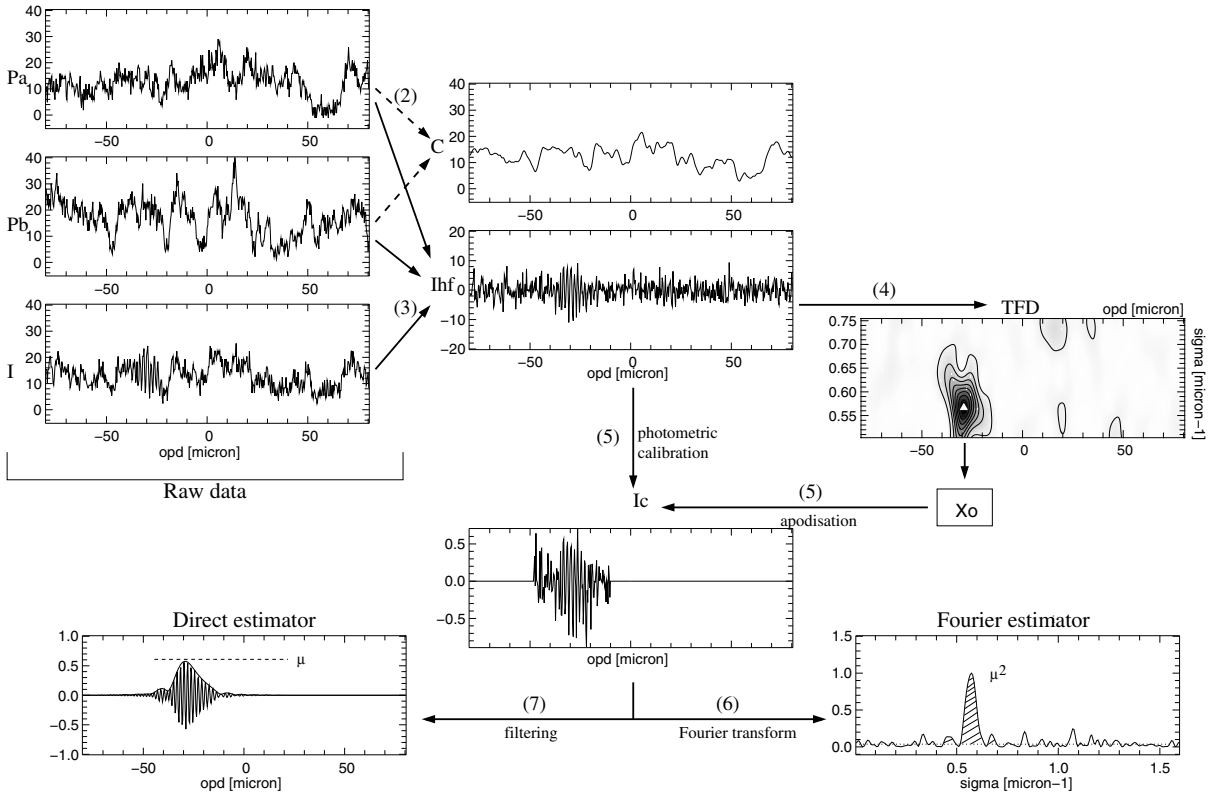


**Fig. 2.** Diagram of the coherence factor data processing. The numbers in brackets refer to the steps detailed in the text (see Sect. 3.2.2).

– $\mu$ is the average of the coherence factor through the spectral response of the interferometer.

To determine $\mu$, we use a data processing similar to the one described by Coude Du Foresto et al. (1997), as follows:

1. we determine the $\widehat{\kappa_a}$ and $\widehat{\kappa_b}$ ratios by Eq. (3);
2. we compute the geometric average of the photometric flux. We use Wiener filtered estimations to minimize the noise amplification in photometric calibration (division by $C$, see step 5):

$$\widehat{C^w} = 2.\sqrt{\widehat{\kappa_a}.\widehat{P_a^w}.\widehat{\kappa_b}.\widehat{P_b^w}}; \tag{7}$$

3. we calculate the highest frequency part of interferometric data. We do not use Wiener filtered estimations of $P_a$ and $P_b$ because these introduce a difference of noise power level between the photometric and other frequencies:

$$\widehat{I_{\rm HF}} = \widehat{I} - \left(\widehat{\kappa_a}.\widehat{P_a} + \widehat{\kappa_b}.\widehat{P_b}\right); \tag{8}$$

4. location of fringes: in order not to add noise that are located far from the interferogram in the OPD space, it is important to apodize $I_{\rm HF}$ around the fringe packet before performing the photometric calibration. We use a Time-Frequency Decomposition ($TFD(\sigma,\tau)$) to find the location of the fringe packet with good accuracy.

$$TFD(\sigma,\tau) = TF_x\left\{\widehat{I_{\rm HF}}(x).\exp\left(-\frac{(x-\tau)^2}{2.\Delta x^2}\right)\right\}. \tag{9}$$

We use $\Delta x = 10$ $\mu$m. We call $\sigma_0$ and $x_0$ the coordinate of the maximum of $|TFD(\sigma,\tau)|$. This method is quite different from the wavelet transform because there is no energy conservation (Ségransan et al. 2003). Thus we cannot determine the coherence directly in this space but it enables us to find fringes that have moved in direct space (optical path delay due to the piston) and in the Fourier space (temporal derivative of the piston);

5. we apodize $I_{\rm HF}$ around $x_0$ and we compute the clean interferogram $\widehat{\mu.I_c}$ only in a small window. We use a $\Delta x' = 40$ $\mu$m window to be sure that the fringes are within the range:

$$\widehat{\mu.I_c} = \frac{\widehat{I_{\rm HF}}}{\widehat{C^w}}.\sqcap_{\Delta x'}(x - x_0); \tag{10}$$

6. we calculate the Power Spectral Density $\widehat{\mu.I_c}^2$ of $\widehat{\mu.I_c}$. After removing the noise power level, the integration of fringe energy gives access to $\widehat{\mu^2}$ (see Coude Du Foresto et al. 1997 for a global explanation of the Fourier estimation). Note that this estimator should be calibrated by the square of the spectral shape of the global transmission.

$$\widehat{\mu^2} = \frac{\int \widehat{\mu.I_c}^2\,\mathrm{d}\sigma}{\int T^2\,\mathrm{d}\sigma}; \tag{11}$$

7. the maximum of the fringe envelope gives access to a direct estimation of $\mu$ without calibration by the spectral shape of the transmission. We calculate this envelope by filtering $\widehat{\mu.I_c}$ around $\sigma_0$ (which we call $\{\widehat{\mu.I_c}\}_{\sigma_0}$) and taking the absolute value.

$$\widehat{\mu} = \max\left(\,|\{\widehat{\mu.I_c}\}_{\sigma_0}|\,\right); \tag{12}$$

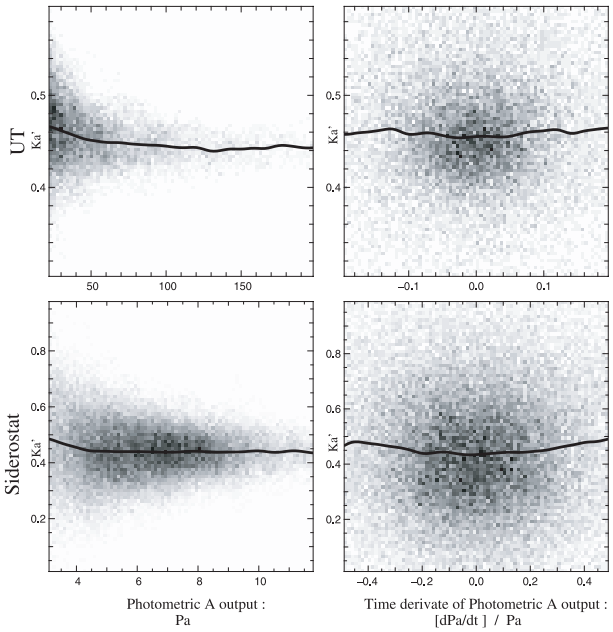


**Fig. 3.** Cross-correlation of $\kappa'_a$ with the estimator of injection: the flux (*left*) and normalized temporal derivative of the flux (*right*). The solid line is the vertical average of the diagram. Note the smaller dispersion of the data with the UTs (*top*) than with the siderostats (*bottom*) due to the smaller photon noise. Each figure corresponds to a BEAM A calibration file of 20 scans (10 840 points) on $\alpha$ Aql.

8. we use this process for all scans of each science acquisition. We call $\left(\left\langle\widehat{\mu^2}\right\rangle\right)^{0.5}$ the *Fourier Visibility Estimator* and $\langle\widehat{\mu}\rangle$ the *Direct Visibility Estimator*, where $\langle\rangle$ denotes an average on the scan. The error of the mean visibility is deduced from the dispersions between all scans divided by the square root of the number of accepted values.

## 4. Results and discussion

### 4.1. Modal filtering

The flux is a measurement of the injection conditions. The increase and decrease of the flux in one beam are due to the motion of a speckle at the fiber input, and a maximum is obtained when the speckle is centered on the fiber axis. To test the modal filtering quality of our component, we use two estimators of the injection conditions:

- $P_a$: the value of the flux, since high flux indicates a good injection and low flux indicates a tilted injection;
- $[\mathrm{d}P_a/\mathrm{d}t]/P_a$: the normalized temporal derivative of the flux that measures the speckle velocity.

We plot the $\kappa'_a$ ratio versus both estimators of injection conditions (Fig. 3) and we compute the average $\kappa'_a$ for each value of $P_a$ and $\mathrm{d}P_a/\mathrm{d}t$ (solid line). There is no evidence for a strong correlation. Since a $Y$ junction is sensitive to the modal distribution in the input waveguide, the non-correlation between $\kappa$ and injection condition allows us to claim that the wavefront is always single-mode before the $Y$ junctions, and therefore that our fibered IO combiner ensures an unbiased modal filtering.

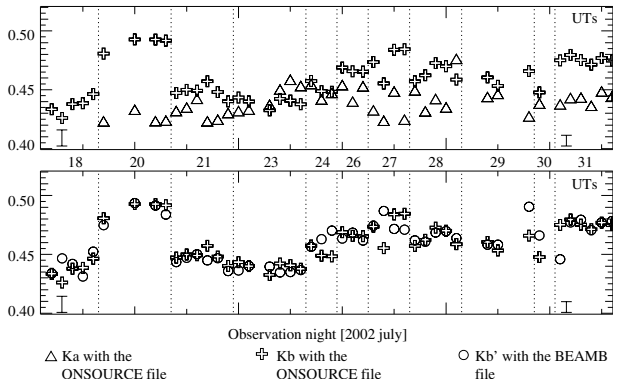


**Fig. 4.** Long time fluctuations of the $\kappa$ ratio on $\alpha$ Aql. Each point represents one observation and vertical lines separate the different nights. The last night was carried out on the Unit Telescopes UT1 and UT2. With the BEAM-B file, $\kappa'_b$ is the average ratio of interferometric on photometric flux. With the ON-SOURCE file, $\kappa_a$ and $\kappa_b$ are estimated at the same time by a linear fit of the interferometric flux with the two photometric ones (see Sect. 3.2.1). The estimated error bars are plotted at the bottom left corner for the siderostats and at the bottom right for the UTs.

**Table 3.** Average flux ratio on $\alpha$ Aql. $\kappa$ is estimated with the ON-SOURCE acquisition (fluctuation fitting) and $\kappa'$ with the BEAM-A/BEAM-B acquisitions. See Sect. 3.2.1 for a global explanation of both methods and see Table 1 for laboratory data.

| Value | Average | rms |
|---|---|---|
| $x$ | $\langle x\rangle$ | $\sigma_x$ |
| $\kappa_a$ | 0.44 | 0.03 |
| $\kappa_b$ | 0.46 | 0.03 |
| $\kappa'_a$ | 0.43 | 0.03 |
| $\kappa'_b$ | 0.46 | 0.04 |
| $\kappa'_a/\kappa_a$ | 1.03 | 0.09 |
| $\kappa_b/'\kappa_b$ | 1.00 | 0.04 |

### 4.2. Stability – Long term fluctuations

For each observation block, we compute the $Y$ junction flux ratio ($\kappa$) with the interferometric acquisition ON-SOURCE and with the two calibration acquisitions BEAM-A and BEAM-B. We summarize the values obtained on $\alpha$ Aql in Fig. 4 and Table 3.

A single-mode excitation corresponds to a flux ratio of 0.5 in the first $Y$ junction. But the reverse $Y$ junction used for combination in the interferometric output introduces optical loss of about 5% maximum which therefore explains both the laboratory and the sky observed values of the $\kappa$ ratio ($\sim$0.45 ± 0.02). In Fig. 4 the variations higher than the error bars correspond to different nights, and so to different alignments. On the same night, the variations can be explained by difference of focus or sensitivity between the detector pixels since the detector support is slightly flexible and moves as a function of the nitrogen load. The two $\kappa$ ratios should be calibrated from night to night.

The $\kappa$ determinations in the interferometric file ON-SOURCE and in the calibration file BEAM-A and BEAM-B are very similar (at the level of ±1%). A systematic

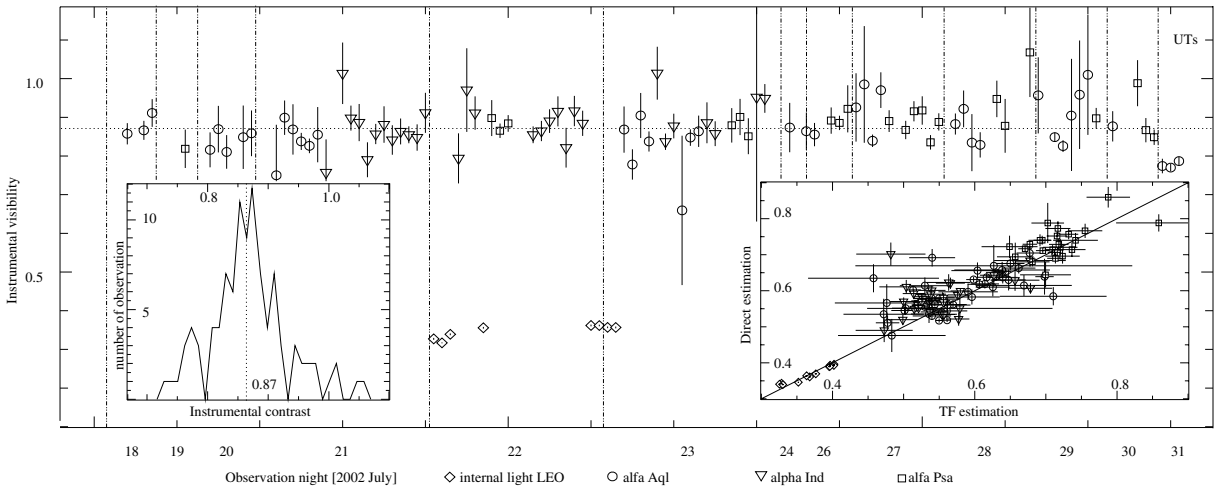


**Fig. 5.** Instrumental visibility with the IONIC component during the different observation nights on 3 calibrators stars ($\alpha$ Aql, $\alpha$ Ind, $\alpha$ Psa) and on the internal light LEONARDO. The last night (31) was carried out with the UTs. The dotted line is the average instrumental visibility on the sky with the siderostats. The histogram is plotted in the left sub-figure. The instrumental visibility is computed with the Fourier visibility estimator. The correlation between the *Direct* and *Fourier* estimator is plotted in the right sub-figure. We assume an effective wavelength of 1.63 $\mu$m and the uniform disk angular diameters of Table 4.

**Table 4.** Instrumental visibility with the IONIC component. We assume that stars are uniform disks and we take an effective wavelength of 1.63 $\mu$m. The angular diameters come from the CHARM database. This table summarizes the values of Fig. 5.

| Target name | ⌀ [mas] | Instrumental visibility |
|---|---|---|
| $\alpha$ Ind | 3.86 | 0.87 ± 0.09 |
| $\alpha$ Aql | 3.12 | 0.86 ± 0.09 |
| $\alpha$ Psa | 2.39 | 0.88 ± 0.05 |
| LEONARDO | – | 0.33 ± 0.06 |

investigation of the different possibilities to recover the photometric channels directly from the interferometric one have been done by the VINCI team. This did not increase the accuracy of the $\kappa$ measurement and this method will not work without turbulence (adaptive optics or internal source) because the fit in Eq. (3) is conditioned by the independent fluctuations of the flux in the two beams

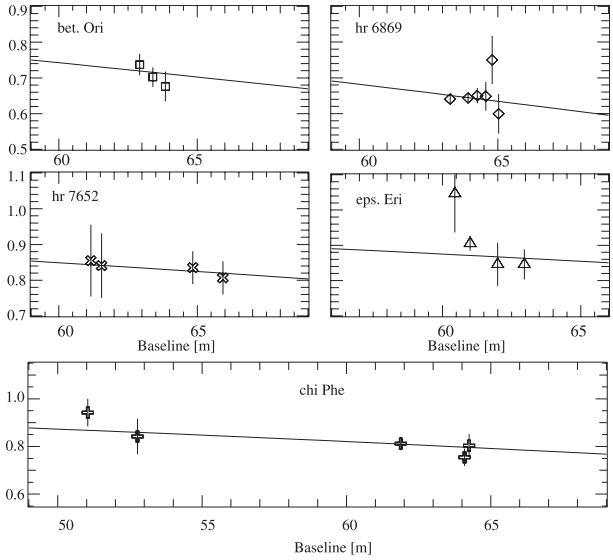


**Fig. 6.** Visibility obtained on different stars corrected for the instrumental visibility (87%) and fitted with the theoretical visibility derived from Table 5 (solid line).

### 4.3. Instrumental visibility

The interferometric efficiency (so-called instrumental visibility or instrumental contrast) is defined as the ratio of the observed visibility and the theoretical visibility. We compute it with the different observations of $\alpha$ Aql, $\alpha$ Ind, $\alpha$ Psa and with the internal light LEONARDO (Fig. 5). We assume an effective wavelength of 1.63 $\mu$m and the uniform disk angular diameters given in Table 4. The average instrumental visibility for each object is summarized in Table 4.

With the internal light LEONARDO, the instrumental visibility is very small (~40%). The same visibility is observed with the MONA fiber combiner. This is due to polarization effects in the beam-splitter between LEONARDO and the combiner table. With the siderostats, the instrumental contrast is stable and reaches 87%, which is just 3% lower than the IONIC combiner test intrinsic visibility. The instrumental contrast with the UTs reaches 78%. A large dispersion in the data is observed in Fig. 5. It corresponds to the statistical dispersion of the visibility calculation, and can be explained by the low flux level for the siderostat data ($SNR < 10$). On the contrary, the errors bars and the dispersion on UTs are much smaller (~2%).

### 4.4. Stellar diameters measurements

We compute the equivalent diameters for five stars observed with the IONIC combiner (Fig. 6 and Table 5). We assume an instrumental visibility of 87 ± 5% and an effective wavelength of 1.63 $\mu$m. For HR 6869, $\epsilon$ Eri and $\beta$ Ori, we found the same

**Table 5.** Angular diameters estimated from the IONIC measurements. We assume an instrumental visibility of 87% and an effective wavelength of 1.63 $\mu$m. The previous measurements are taken from the CHARM database. LBI is for *Long Baseline Interferometry* and SPE for *SPectroscopic Estimation*.

| Target name | ⌀ [mas] | Previous measurement |
|---|---|---|
| HR 6869 | 3.1 ± 0.1 | 2.98 ± 0.03 (SPE) |
| $\beta$ Ori | 2.8 ± 0.1 | 2.77 ± 0.03 (LBI) |
| $\chi$ Phe | 2.3 ± 0.2 | 2.69 ± 0.06 (SPE) |
| HR 7652 | 2.2 ± 0.2 | 2.69 ± 0.03 (SPE) |
| $\epsilon$ Eri | 2.0 ± 0.2 | 2.15 ± 0.06 (SPE) |

diameter as previous measurements. For $\chi$ Phe and HR 7652, we found quite different diameters than the spectroscopic estimations.

### 4.5. Sensibility

The accuracy of the mean visibility depends on the total coherent flux collected during the acquisition. Since the observation conditions were not similar for all files, we plot the relative error of the main visibility for each file versus the total coherent flux normalized to a reference file (100 scans on $\alpha$ Aql with the siderostats, $\mu = 0.7$). This file corresponds to a correlated magnitude of $mH_{\rm Corr} = 0.8$, which is the effective magnitude of the fringe part of the measured signal. This magnitude is defined as:

$$mH_{\rm Corr} = -2.5\ \log\left(10^{\frac{-mH}{2.5}}.\mu^2\right). \quad (13)$$

In Fig. 7, we see that the accuracy increases with the total coherent flux collected by the siderostats. The minimum relative error on the square visibility of the IONIC combiner on the sky is about 2%. Since the coherent flux is similar, the relative error on $\alpha$ Aql with UTs is much larger than the one obtained on the internal light. This is due to the atmospheric optical path delay which damages the power spectral density. A relative accuracy of 10% was obtained for a coherent flux equivalent to 0.15 times the reference file. It corresponds to a correlated magnitude of $mH_{\rm Corr} = 2.8$. In agreement with this, the faintest star observed with the siderostats during the run was $\kappa 2$ Scl ($mH = 2.47$).

To determine the accuracy of IONIC with the UTs without adaptive optics (AO), we will use a comparison with the MONA fibered combiner. Because the 2 combiners are exactly in the same environment, we can expect that they have the same difference of efficiency between siderostats and UTs. With MONA, a relative accuracy of 10% with 100 scans is obtain for a $mK_{\rm Corr} = 4.3$ with the siderostats. On the other hand, the faintest star observed with the UTs without AO is HD 112282 ($mK = 7.7$, $\mu^2 \sim 1$ and accuracy about 3% for 100 scans). It gives a difference of 3.4 mag. Thus, fringes on an unresolved star with $mH \sim 6$ could be record with the IONIC combiner and the UTs.

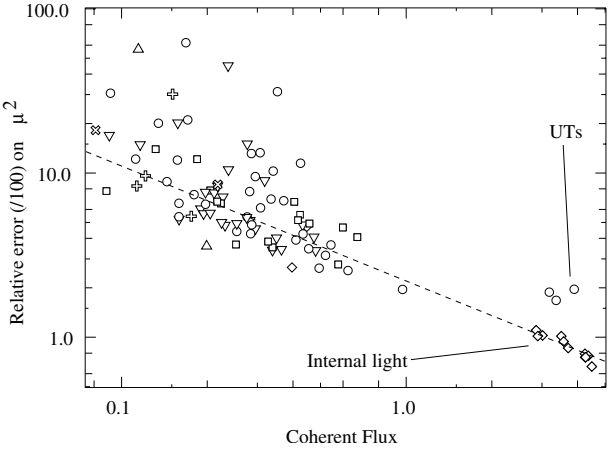


**Fig. 7.** Relative error in % of the mean visibility with the IONIC combiner versus the total coherent flux collected during the acquisition. $X$-axis units have normalized by the flux obtained on the best siderostat file (100 scans on $\alpha$ Aql with a visibility of 0.7). The dash line represents a linear fit. The marker used are the same as for Fig. 4.

An optimization of the injection optics of VINCI to adapt them to the numerical aperture of the IONIC fiber could increase the sensitivity of the combiner by 50%. Note that this run was not performed to determine the limiting magnitude of IONIC.

## 5. Conclusions and perspectives

In this paper we present results obtained with the Very Large Telescope Interferometer Commissioning Instrument where the fiber interferometric coupler has been temporally replaced by an integrated optics beam combiner.

The VLTI has now access to the $H$-band for the commissioning and the scientific exploitation of a two-beam combination. The "plug and play" ability of IONIC allows one to switch easily between the $K$ and the $H$ band combiner without additional opto-mechanical changes. It is thus possible to do interferometric observations of the same object in the two bands at the VLTI site within a short time. The spatial resolution of the VLTI is increased by a factor of 1.38 by using the shorter wavelength of the $H$ band. The global intrinsic visibility of the total VLTI+IONIC optical train is better than 85%. The IONIC component ensures the combination with a good stability and unbiased photometric calibration which is necessary to determine the coherence factor with accuracy. The star diameter measurements are in agreement with previous ones. The best precision obtained on the visibility measurement is ~2%. The accuracy is limited by the photon noise in the siderostats and by the atmospheric piston for the UTs. We extrapolate that a magnitude $mH \sim 6$ could be observed and processed with the UTs without adaptive optics. This allows us to measure visibility with a good accuracy, and so to detect features significantly smaller than the object angular extension.

Currently, the accuracy of the coherency measurement of IONIC is limited by the low flux in the instrument (a factor of 2 mag between the VLTI throughput in $H$ and $K$) and by the larger turbulence in $H$ which reduces the efficiency of the

photometric calibration. Some changes can strongly increase the performances of the actual two-beams IONIC combiner. First, an optimization of the injection optics of VINCI to adapt them to the numerical aperture of the IONIC fiber will increase the flux in the combiner by a factor of 1.5. Also, it is possible to directly image the output of the combiner on the detector. This solution avoids flux loss due to the output fibers and connections. Finally, the reverse *Y*-junction of the current IONIC combiner can be replaced by a coupler with two outputs in phase opposition. This will increase the coherent flux by a factor 2 (see Eq. (6)) and simplify the fringe tracking and the continuum removal in the data processing.

It appears that integrated optics is a promising solution for the imaging mode of near-infrared interferometers (*J* to *K* bands) with a large number of baselines (Kern et al. 2003). The compactness of the planar optical component allows one to combine many beams in the same chip, which drastically reduces the instability and the required alignments. The observational strategies (number of baselines, wavelength, combination scheme...) can be adapted to the object thanks to the "plug and play" ability of IONIC combiners. Output beams of the planar component can act as the input slit of a spectrograph, avoiding complex anamorphic optics. Since integrated optics provides not only all the usual optical functions but also diffracting and dephasing ones, it is possible to produce a coaxial combination (like VINCI) as well as a multi-axial combination scheme (like AMBER). Thus, we propose this technique to combine the 8 telescopes of the entire VLTI array. The design of an IONIC chip to simultaneously combine four telescopes is already available.

*Acknowledgements.* The authors want to thank Laurence Glück, Eric Tatulli and the ESO support for the observations. All the calculations and graphics were performed with the free software Yorick. This work is based on observations made with the European Southern Observatory telescopes obtained from the ESO/ST-ECF Science Archive Facility. This research has also made use of the SIMBAD database at CDS, Strasbourg (France).

## References

Berger, J., Haguenauer, P., Kern, P. Y., et al. 2003, in Interferometry for optical astronomy II, ed. Wesley A. Traub, Proc. SPIE, 4838, 1099

Berger, J. P., Haguenauer, P., Kern, P., et al. 2001, A&A, 376, L31

Coude Du Foresto, V., Ridgway, S., & Mariotti, J.-M. 1997, A&AS, 121, 379

di Folco, E., Kervella, P., Thevenin, F., et al. 2003, in IAU Symp., in press

Domiciano de Souza, A., Kervella, P., Jankov, S., et al. 2003, A&A, 407, L47

Glindemann, A., Algomedo, J., Amestica, R., et al. 2003, in Interferometry for optical astronomy II, ed. Wesley A. Traub, Proc. SPIE, 4838, 89

Haguenauer, P., Severi, M., Schanen-Duport, I., et al. 2000, in Interferometry in optical astronomy, ed. P. J. Lena, & A. Quirrenbach, Proc. SPIE, 4006, 1107

Kern, P. Y., Malbet, F., Berger, J., et al. 2003, in Interferometry for optical astronomy II, ed. Wesley A. Traub, Proc. SPIE, 4838, 312

Kervella, P., Gitton, P. B., Segransan, D., et al. 2003a, in Interferometry for optical astronomy II, ed. Wesley A. Traub, Proc. SPIE, 4838, 858

Kervella, P., Thévenin, F., Morel, P., Bordé, P., & Di Folco, E. 2003b, A&A, 408, 681

Leinert, C., Graser, U., Waters, L. B. F. M., et al. 2003, in Interferometry for optical astronomy II, ed. Wesley A. Traub, Proc. SPIE, 4838, 893

Malbet, F., Kern, P., Schanen-Duport, I., et al. 1999, A&AS, 138, 135

Petrov, R. G., Malbet, F., Weigelt, G., et al. 2003, in Interferometry for optical astronomy II, ed. Wesley A. Traub, Proc. SPIE, 4838, 924

Pijpers, F. P., Teixeira, T. C., Garcia, P. J., et al. 2003, A&A, 406, L15

Richichi, A., & Percheron, I. 2002, A&A, 386, 492

Ségransan, D., Kervella, P., Forveille, T., & Queloz, D. 2003, A&A, 397, L5